Journal of RAMAN SPECTROSCOPY WILEY

Ultraviolet resonance Raman spectroscopy of anthracene: Experiment and theory

Tim Holtum[1] | Julien Bloino[2] | Christos Pappas[1] | Vikas Kumar[1] |
Vincenzo Barone[2] | Sebastian Schlücker[1]

[1]Department of Chemistry, Center for Nanointegration Duisburg-Essen (CENIDE), University of Duisburg-Essen, Essen, Germany

[2]SMART Laboratory, Scuola Normale Superiore, Pisa, Italy

Correspondence
Julien Bloino and Vincenzo Barone, SMART Laboratory, Scuola Normale Superiore, Piazza dei Cavalieri 7, I-56126 Pisa, Italy.
Email: julien.bloino@sns.it; vincenzo.barone@sns.it

Sebastian Schlücker, Department of Chemistry, Center for Nanointegration Duisburg-Essen (CENIDE), University of Duisburg-Essen, Universitätsstraße 5, D-45141 Essen, Germany.
Email: sebastian.schluecker@uni-due.de

Abstract

Ultraviolet resonance Raman (UVRR) scattering is a highly sensitive and selective vibrational spectroscopic technique with a broad range of applications from polyaromatic hydrocarbons (PAHs) to biomolecular systems (peptides/proteins and nucleic acids) and catalysts. The interpretation of experimental UVRR spectra is not as straightforward as in purely vibrational Raman scattering (Placzek approximation) due to the involvement of higher lying electronic states and vibronic coupling. This necessitates the comparison with theoretical UVRR spectra computed by electronic structure calculations. Anthracene is an ideal model system for such a comparison between experiment and theory because it is rigid, symmetric, and of moderate size. By taking into account Herzberg–Teller contributions including Duschinsky effects, bulk solvent effects, and anharmonic contributions, a good qualitative agreement close to the resonance condition is achieved. The present study shows that within the framework of time-dependent density functional theory (TD-DFT), a general and robust approach for the analysis and interpretation of resonance Raman spectra of medium- to large-size molecules is available.

KEYWORDS

chemical calculations, polyaromatic hydrocarbon, Raman spectroscopy, resonance Raman, UVRR

1 | INTRODUCTION

Ultraviolet resonance Raman (UVRR) scattering[1–4] is a vibrational spectroscopic technique which provides both high sensitivity and selectivity: if the laser excitation wavelength matches an electronic resonance, that is, overlaps with a peak in the UV absorption spectrum, it results in a Raman signal enhancement by several orders of magnitude only for normal modes of the corresponding UV chromophore compared with normal, electronically off-resonant Raman scattering. Due to these two advantages, UVRR spectroscopy has been applied to studying a broad range of molecular systems and materials, ranging from polyaromatic hydrocarbons (PAHs),[5] aromatic amino acids,[6–8] and nucleotides[2] to peptides/proteins[9,10] and nucleic acids.[11,12]

Tim Holtum and Julien Bloino contributed equally to this study.

Applications in chemistry include the UVRR spectroscopic characterization of artificial supramolecular ligands and their molecular recognition of peptides and proteins[13–17] as well as the characterization of catalysts.[18,19]

Generally, the assignment of peaks in vibrational Raman spectra is assisted by a normal mode analysis. Nowadays, density functional theory (DFT) in combination with sufficient computational resources is capable of predicting the vibrational Raman spectra even of complex polyatomic molecules. Routine DFT calculations are performed within the harmonic approximation (Hessian matrix) for molecules in the gas phase. The calculation of Raman spectra usually requires analytical calculations of the force constants k_i as the second derivative of the corresponding harmonic potentials $V_i = k_i \cdot R_i^2$. Further, solvent effects are routinely included by continuum models such as polarizable continuum models (PCMs)[20,21] or, computationally more demanding, by the inclusion of explicit solvent molecules. Empirical scaling factors are routinely applied to the calculated harmonic wavenumbers for comparison with experimental values inherently affected by anharmonicity. A physically more meaningful approach considers anharmonic effects on both vibrational wavenumbers and Raman intensity.[22–24] Such anharmonic calculations require significantly more computational resources, but normally yield a good agreement with experimental vibrational Raman spectra, and can recover the nonfundamental features (overtones and combination bands) present in the experimental band shape.

In resonance Raman (RR) scattering, the vibrational wavenumbers are the same as in normal Raman scattering (cf. fig. 4.2, p. 56, in Long[25]); that is, we are not considering normal pure electronic or normal pure vibronic Raman scattering (cf. fig. 4.7, p. 78, in Long[25]). In contrast to normal Raman scattering, the computation of RR intensities is more complex. Standard formulations of Raman scattering assume the far-from-resonance regime, which allows a significant simplification of the Kramers–Heisenberg–Dirac dispersion relation (Placzek pure vibrational transition polarizability). However, this radical simplification is not applicable in the case of an electronic resonance and a suitable formalism must be chosen. This can be done at a pure electronic level, as done by Jensen et al.[26] However, in resonance conditions, subtle variations in the incident energy will change the overlap conditions at the vibrational levels. Hence, a proper account of the vibrational structure in the intermediate state is crucial. This is even more relevant for systems exhibiting high symmetry, because the transition probabilities depend not only on the symmetry of the electronic transition dipole moment but also on

the initial and final vibrational states. The most cost-effective calculations to account for the vibronic structure are based on the Franck–Condon (FC) principle.[27–29]

Benchmarking the performance of computational approaches to experimental RR spectra necessitates the choice of a well-suited chromophore as a model system, which is neither too simple nor too complex and therefore computationally too demanding. For various reasons, PAHs such as naphthalene and anthracene are very well suited for this purpose. They are relatively small, rigid molecules with a high symmetry and a delocalized π-electron system. The rigidity simplifies the computation of vibronic spectra based on sum-over-states formulations as a relatively low number of transitions contribute significantly to the spectrum. This is also why they have often been used to validate implementations on FC-based vibronic calculations.[30–33] In general, the high symmetry leads to a number of observable overtone and combination bands in the vibrational spectra, which can be analyzed.[34,35] An important feature of interest in the present study is that the delocalized π-electron system makes them highly Raman active. Last but not least, PAHs are also of fundamental interest because, in addition to their natural abundance in fossil fuels and their generation in anthropogenic processes, they are also an integral component of interstellar matter.[36,37]

We decided to select anthracene because it exhibits only one dominant electronic excitation in the UV region around 251 nm arising from the S_0 to S_9 transition (Figure 1). The presence of only a single isolated electronic resonance simplifies the vibronic UVRR intensity analysis. Overall, these molecular properties make anthracene an excellent model system for comparing experimental UVRR spectra with computational results.

Specifically, we first compared the experimental UV absorption spectrum to DFT-computed one-photon absorption spectra to validate the quality of the electronic structure calculation method. This step was also important to confirm the correct resonance conditions to use in
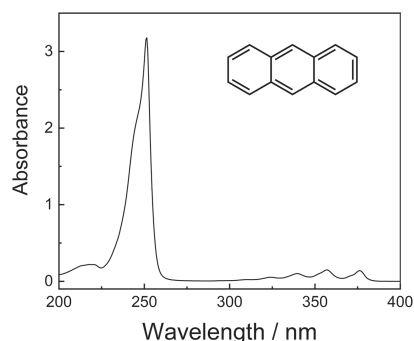

FIGURE 1 UV absorption spectrum of anthracene (100 μM in acetonitrile) together with the molecular structure of anthracene

the theoretical UVRR spectrum. Different refinements in FC-based vibronic calculations are possible, so we then compared the experimental UVRR spectrum excited right at the electronic resonance ($\lambda_{max} = \lambda_{exc} = 251$ nm) with DFT-computed UVRR spectra at different levels of theory (FC fundamentals vs. FC and Herzberg–Teller (FCHT) fundamentals vs. FCHT incl. overtones/combinations vs. FCHT with anharmonic corrections, where FCHT refers to the inclusion of both FC terms and the Herzberg–Teller (HT) extension in vibronic calculations) to identify the level of theory best suited for describing the features observed in the experimental UVRR spectrum. Finally, UVRR excitation spectroscopy in the range 244–253 nm was performed, and the corresponding UVRR spectra are compared with the corresponding DFT-computed UVRR spectra for these different electronic resonance conditions.

2 | RESULTS AND DISCUSSION

Let us first consider the one-photon absorption spectrum, an important step to calibrate the resonance conditions for both experiment and theory. Figure 2 shows the normalized experimental and calculated UV absorption spectrum of anthracene in the range 37,000–47,000 cm^{-1} ($\sim$270–213 nm). In the experimental spectrum (black), the absorption maximum is observed around
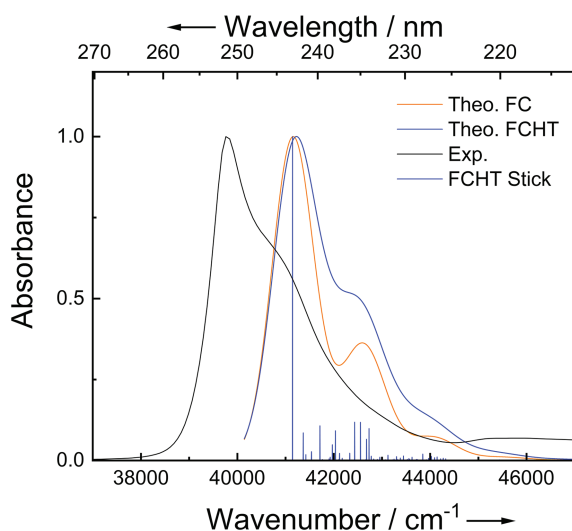
FIGURE 2 Calculated one-photon absorption spectrum at Franck–Condon (FC) (orange) and FC and Herzberg–Teller (FCHT) (blue) level compared with the experimental UV absorption spectrum (black). The experimental broadening was simulated by mean of Gaussian distribution functions with half widths at half maximum of 500 cm^{-1}

$\tilde{\nu}_{max} = 39,800$ cm^{-1} ($\sim$251 nm) with a shoulder on the higher energy/lower wavelength side. This characteristic is also reflected in both DFT-computed vibronic spectra at the FC (orange) and FCHT (blue) levels. The overall horizontal offset of $\sim$1400 cm^{-1} (or 10 nm) between the experimental and computed UV absorption spectra is considered to be relatively small for TD-DFT calculations of this type. For both FC and FCHT, the main peak is closely centered on the 0–0 transition, between the vibrational ground states of the S_0 and S_9 electronic states. Although the computed band shapes are in good agreement with experiment, the shoulder at the FCHT level is closer to the experimental one, which confirms the importance of the HT contributions. This is expected, because the oscillator strength for the $S_0 \rightarrow S_9$ transition is low ($f = 0.031$), which means that the electronic transition dipole moment and its derivatives are of similar order of magnitude. The shoulder is due to multiple transitions, mainly $|0\rangle \rightarrow |1_{41}\rangle$, $|0\rangle \rightarrow |1_{46}\rangle$, and $|0\rangle \rightarrow |1_{55}\rangle$, all of a_g symmetry (the subscript refers to the normal mode). The corresponding eigenvectors of these three normal modes are shown in Figure 4 (top right and bottom left and right).
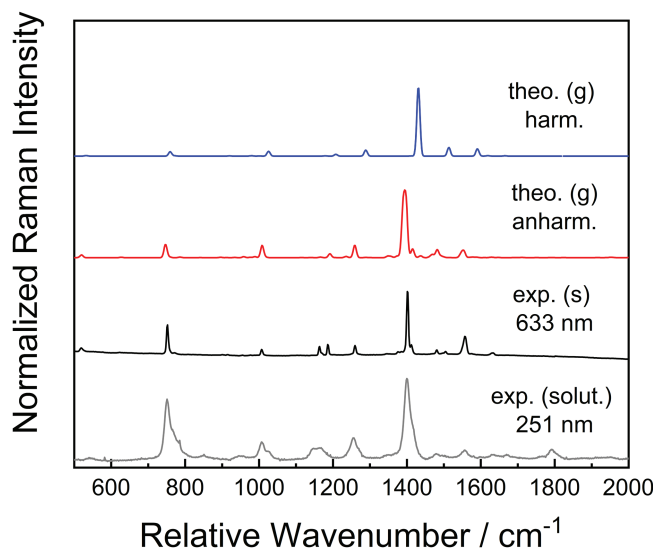
These results confirm the good quality of the selected electronic structure calculation method. For full resonance conditions, the energy of the 0–0 transition was used, which exhibits a shift of 1464 cm^{-1} between the experimental and theoretical maxima. This shift will be systematically added to the experimental incident laser energy.

Anthracene ($C_{14}H_{10}$) is planar with D_{2h} symmetry and 66 normal modes. Each normal mode transforms as one of the four irreducible representations of the D_{2h} molecular point group:
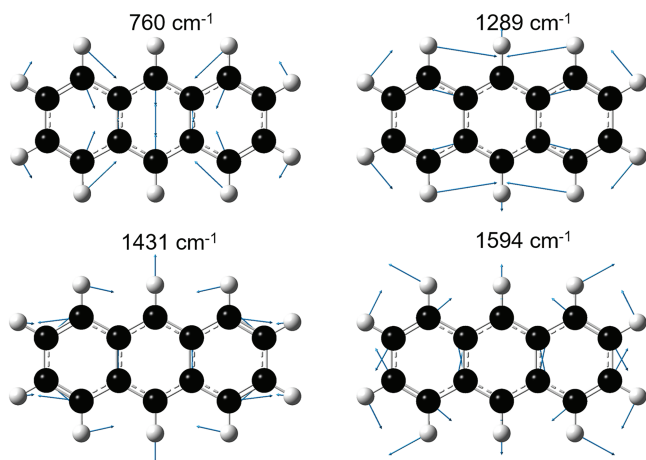
$$12\,a_g + 11\,b_{3g} + 11\,b_{1u} + 11\,b_{2u} + 4\,b_{1g} + 6\,b_{2g} + 5\,a_{1u} + 6\,b_{3u}.$$

Due to the presence of a center of inversion (i), the mutual exclusion principle is applicable: normal modes are either Raman active (g modes: +1 for i in character table) or IR active (u modes: −1 for i in character table). Thus, out of the 66 normal modes, 33 are Raman active (12 a_g + 11 b_{3g} + 4 b_{1g} + 6 b_{2g}) and 28 are IR active (11 b_{1u} + 11 b_{2u} + 6 b_{3u}). The five a_{1u} modes are neither Raman nor IR active because there is no change in both polarizability and dipole moment when passing through the equilibrium position. Among the 33 Raman-active modes, there are 12 totally symmetric modes (a_g) and 21 nontotally symmetric modes (11 b_{3g} + 4 b_{1g} + 6 b_{2g}). The a_g and b_{3g} modes are in-plane modes (+1 for σ_{yz} in character table), whereas the b_{1g} and b_{2g} modes are out-of-plane modes (−1 for σ_{yz} in character table).

Figure 3 depicts theoretical and experimental Raman spectra of anthracene in the fingerprint region (500–2000 cm^{-1}). The theoretical normal Raman spectrum computed within the harmonic approximation is shown in blue. The dominant peak at 1431 cm^{-1} can be assigned to a totally symmetric (a$_g$) in-plane mode with strong CC stretching motions (cf. Figure 4, bottom left). Also, the peaks at 760, 1289, and 1591 cm^{-1} are a$_g$ modes and therefore in-plane modes: two breathing modes involving either all three phenyl rings (cf. Figure 4, top left) or dominantly the central phenyl ring (cf. Figure 4, top right) as well as a CC stretching delocalized over all three phenyl rings (cf. Figure 4, bottom right). Except for the peak at 1208 cm^{-1} (b$_{3g}$ mode), all the modes observable in the theoretical spectrum are a$_g$ modes. The theoretical normal Raman spectrum computed with anharmonic corrections is shown in red. As expected, the dominant peaks discussed above are all shifted to smaller wavenumber values: $760 \rightarrow 747$, $1208 \rightarrow 1192$, $1289 \rightarrow 1258$, $1431 \rightarrow 1394$, and $1594 \rightarrow 1552$ cm^{-1}. In addition to the harmonic approximation, in which only fundamental transitions are considered, now also overtones and combination bands can be observed, for example, the shoulder at 1415 cm^{-1} next to the dominant peak at 1394 cm^{-1}. This shoulder is also observed in the normal Raman spectrum of anthracene in the solid state (black) at 1412 cm^{-1} next to the dominant peak at 1402 cm^{-1}. Obviously, anharmonic corrections are necessary to be included for obtaining a satisfactory agreement between theory and experiment with respect to peak positions and number of peaks. Finally, the UVRR spectrum of anthracene in acetonitrile is shown in gray. The solvent peaks are subtracted. The raw data for the experimental UVRR spectrum including the Raman peaks from the solvent acetonitrile are shown in Figure S3. In comparison with the electronically off-resonant normal Raman spectrum (black), the UVRR spectrum (gray) exhibits different relative Raman intensities. For certain normal modes, the signal enhancement upon resonant excitation is significantly higher than for others. For example, the overtone/combination band at 1791 cm^{-1} in the UVRR spectrum (gray) is now detectable, whereas in the theoretical anharmonic normal Raman spectrum (red), it has only a vanishingly small intensity and cannot be detected under electronically off-resonant conditions (black). A second example is the region around the intense band at 752 cm^{-1} where, in addition to the intensity increase of the central peak, a shoulder at higher wavenumbers can be observed; the latter is assigned to fundamental transition, which is barely observable at 771 cm^{-1} in the experimental off-resonant spectrum (black) and is not resolved in the UVRR spectrum due to the lower spectral resolution compared with vis Raman spectrum.

Figure 5 compares the experimental UVRR spectrum (bottom) with the vibronic UVRR spectra computed with different methods (see computational details): FC fundamentals, FCHT fundamentals, FCHT fundamentals plus overtones and combinations, and finally the latter with additional anharmonic corrections to the wavenumber. The theoretical spectrum with the FC method exhibits exclusively a$_g$ modes, which are enhanced upon resonant

FIGURE 3 Comparison of density functional theory (DFT)-computed normal Raman and experimental Raman spectra of anthracene: (blue) theory harmonic approximation with polarizable continuum model (PCM) acetonitrile; (red) theory anharmonic corrections with PCM acetonitrile; (black) experiment, solidstate (s), laser excitation at 633 nm; and (gray) experiment, 100 μM in acetonitrile with solvent peaks subtracted, laser excitation at 251 nm. The presentation of the theoretical spectra of a Lorentzian profile with a half width at half maximum (HWHM) of 5 cm^{-1} was chosen
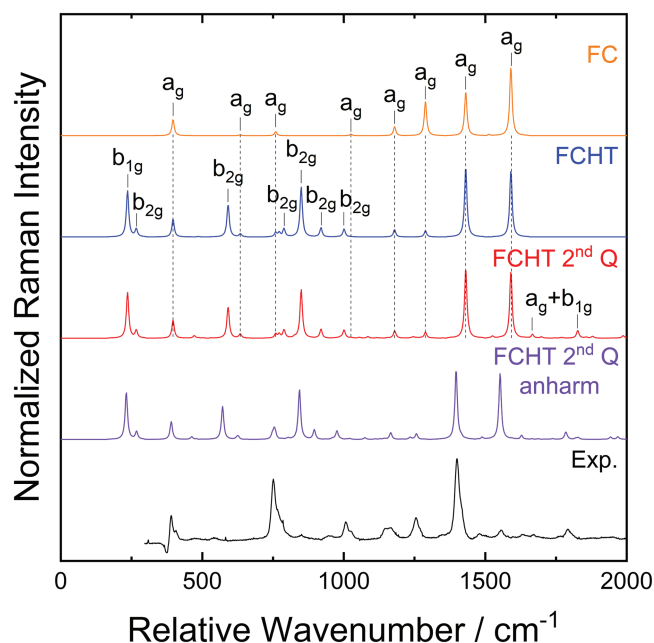

FIGURE 4 Eigenvectors of selected normal modes

FIGURE 5 Calculated ultraviolet resonance Raman (UVRR) spectra with Franck–Condon (FC) (orange), FC and Herzberg–Teller (FCHT) (blue), FCHT with inclusion of a second vibrational quanta (red), and FCHT with second vibrational quanta and anharmonic wavenumber correction (violet) compared with the experimental UVRR spectrum excited at 251 nm (black). Theoretical broadening by mean of Lorentzian distribution functions with half widths at half maximum of 5 cm^{-1}

excitation. This is expected, as the FC method assumes the electronic transition dipole moment to be constant, equivalent to the A term in Albrecht's theory of Raman intensities.[38]

In contrast, the theoretical spectrum computed with the FCHT method exhibits also nontotally symmetric modes (b_{1g}, b_{2g}, and b_{3g}) with intensities comparable with those of the a_g modes. The enhancement of nontotally symmetric modes via HT effects in vibrational RR coupling (see chapter 4.8, p. 68f, in Long[25]) is expected from the B, C, and D terms in Albrecht's theory, which include the corresponding coupling integrals (cf. eq. 4.8.5, p. 69, in Long[25]). The intensities of the nontotally symmetric modes are comparable with those of the totally symmetric modes because the $S_0 \rightarrow S_9$ transition has a very low oscillator strength and the derivatives of the electronic transition dipole moments with respect to the normal coordinates are of similar order of magnitude as the reference electronic transition dipole moments.

In addition to the fundamental transitions, also all overtones and combination bands were calculated with the FCHT method (FCHT second Q). Most notably, two $a_g + b_{1g}$ combination modes are observed as additional

peaks at 1666 and 1826 cm^{-1}. The latter one matches the peak at 1794 cm^{-1} in the experimental UVRR spectrum.

Finally, the anharmonic corrections to wavenumbers for the fundamental transitions were calculated with the FCHT method. This yields an excellent agreement of the peak positions in the calculated and experimental UVRR spectra. For example, the deviation for the most dominant peak is only a few cm^{-1}: 1401 cm^{-1} (exp.) vs. 1396 cm^{-1} (theo. anharmonic) compared with 1432 cm^{-1} in the harmonic approximation.

However, for the intensities, the deviation between experiment and theory is larger. With the inclusion of FCHT, the intensity of the dominant band at 1430/1396 cm^{-1} increases, but the band at 1590/1560 cm^{-1} still shows an intensity comparable with the band at 1430/1396 cm^{-1}, which is not reflected in the experimental spectrum. Similarly, applying the anharmonic correction increases the intensity of the band at 760/755 cm^{-1}, but the intensity is still considerably lower than expected from the experiment. We attribute these parts of disagreement to the general problems of TD-DFT to accurately describe higher excited states such as S_9 here, which leads to discrepancies in the calculation of the corresponding transition integrals.

UVRR excitation spectroscopy across the resonance of anthracene at 251 nm was performed in the range of 244 to 253 nm. For wavelengths between 253 and 263 nm, that is, near the second harmonic at 258 nm of pump beam at 515 nm, the laser power drops down significantly, which prevents an extension to longer wavelengths. From 244 to 248 nm, the excitation wavelength was moved in steps of 2 nm and from 248 to 253 nm in steps of 1 nm to have more spectra near the resonance. The measured UVRR spectra of a anthracene (100 µM in acetonitrile) in the range from 500 to 2000 cm^{-1} are shown together with the computed vibronic UVRR spectra in Figure 6 in black and blue, respectively. All spectra are normalized to the acetonitrile C≡N stretching peak at 2250 cm^{-1} (not displayed; see Figure S3). The corresponding Raman excitation profile for the 755, 1258, 1405, and 1561 cm^{-1} can be found in Figure S8. In addition, the Raman spectrum of the solvent acetonitrile is displayed on the bottom with peaks around 918, 1375, and 1443 cm^{-1}, which interfere little with the UVRR spectrum of anthracene.

At an excitation wavelength of 253 nm slightly above the resonance, the UVRR spectrum shows the same basic features observed in the resonance condition, albeit with lower intensities. The shoulders of the 1400 cm^{-1} are attributed to the solvent. Decreasing the laser excitation wavelength first leads to an increase for all peaks until the resonance condition is fully met at 251 nm. Moving to lower excitation wavelengths, we observe a decrease in
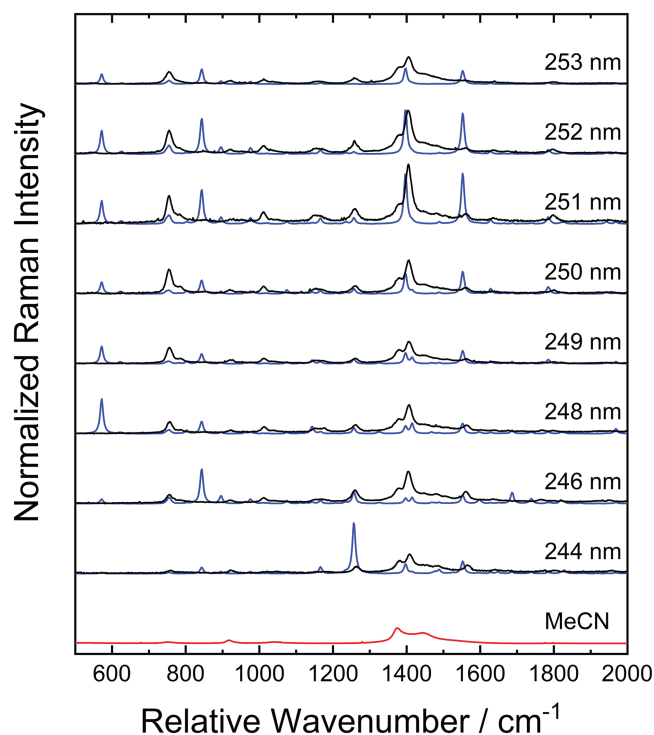
FIGURE 6 Calculated ultraviolet resonance Raman (UVRR) spectra with Franck–Condon and Herzberg–Teller (FCHT) with second vibrational quanta and anharmonic wavenumber correction (blue) compared with the experimental UVRR spectrum at several excitation wavelengths between 244 and 253 nm (black). Theoretical broadening by mean of Lorentzian distribution functions with half widths at half maximum of 5 cm^{-1}. Raman spectrum of the solvent acetonitrile on the bottom (red)

intensity until the excitation at 249 nm. Going to 248 and 246 nm, the peaks around 1259, 1405, and 1561 cm^{-1} increase, which are associated with the $|0\rangle \rightarrow |1_{41}\rangle$, $|0\rangle \rightarrow |1_{46}\rangle$, and $|0\rangle \rightarrow |1_{55}\rangle$ transitions, respectively. These were also identified as the transitions mainly responsible for the lower wavelength shoulder in the one-photon absorption spectrum (cf. Figure 2). Upon decreasing the excitation wavelength to 244 nm, the Raman intensity of all peaks decreases. For the calculated spectra, the systematic increase and decrease of all Raman bands are also observed when shifting the excitation wavelength from 253 to 250 nm. Moving to lower excitation wavelengths, the intensity of the Raman bands overall decreases, except for single bands increasing around a certain excitation wavelength. At 248 nm, the band at 572 cm^1 is increased; at 246 nm, the band at 844 cm^{-1} is increased; and at 244 nm, the band at 1256 cm^{-1} is increased. These wavenumber values roughly match the wavenumber shift from the resonance; for example, at 244 nm, the wavenumber shift is about 1143 cm^{-1} assuming resonance at 251 nm.

Overall, the qualitative agreement between experimental and calculated UVRR spectra is good close to the resonance, but loses quality at lower wavelengths, when vibronic coupling becomes more relevant.

3 | CONCLUSIONS

In this paper, we have presented RR spectra recorded for anthracene in different solvents and interpreted by means of a general computational approach devised to take the most significant stereo-electronic, vibrational, and environmental effects into proper account. In general terms, the agreement between experimental and computed spectra is very satisfactory when the refined theoretical models like HT contributions, including Duschinsky effects, bulk solvent effects, and anharmonic contributions to wavenumbers, are included. However, further developments can be envisaged to improve the quality of the computations. The most obvious step is to improve the theoretical accuracy of the excitation energies. In the present case, the experimental band, centered on the 0–0 transition, is quite easy to be detected, so that a simple shift procedure can be applied to computed spectra. However, in more complex cases, more advanced electronic structure calculation methods (e.g., CASPT2 and EOM-CC) can be employed to perform single-point evaluations of transition energies at DFT geometries.[39] A more difficult issue is related to the inclusion of anharmonic contributions also in the evaluation of FC (and HT) couplings between the vibrational states of the ground and intermediate electronic states. For large molecules, a brute-force approach to this problem would be prohibitive, but integration of the sum-over-state model employed in the present study and the purely electronic approach followed by Jensen et al.[26] (for which anharmonic intensities are not too difficult to evaluate) represents an interesting and effective perspective. A related issue is the treatment of flexible molecules showing large-amplitude vibrational modes. Here, the problem is the same for both resonant and normal Raman spectra, and effective solutions are already available for single large-amplitude motions only weakly coupled to the other small-amplitude motions.[40] More general situations require further developments and effective implementations. Another aspect is the proper treatment of situations between far and at-resonance regimes. Finally, the presence of several low-lying excited states (here we examined the $S_0 \rightarrow S_9$ transition) in near resonance with the laser frequency adds further complications, which should be properly treated. Although this represents welcome paths of improvements for theory to support experiment with a high level of reliability, the

results of the present study show that we already dispose of a general and robust approach for the analysis and interpretation of RR spectra of medium- to large-size molecules.

4 | MATERIALS AND METHODS

UV laser wavelengths in the wavelength range from 244 to 253 nm were obtained by a continuously tunable picosecond pulsed laser system (Light Conversion; PHAROS, SHBC, ORPHEUS-PS, and LYRA). A more detailed description of this laser system can be found elsewhere.[41] In brief, a bandwidth-compressed second harmonic output of a Yb:KGW laser pumped a multistage picosecond optical parametric amplifier (OPA; ORPHEUS-PS). Subsequently, the two consecutive second harmonic generations of the OPA output provided the tunable UV pulses. Liquid samples were kept in a fused silica cuvette (internal dimensions: 2×10 mm). The UV laser was focused into the sample along the light path of the cuvette (10 mm). The scattered Raman signal was collected in a $90°$ geometry by a concave mirror ($f = 18$ mm) and focused into a spectrometer (Acton Research Corp.; SpectraPro-500i, grating with 2400 grooves/mm, f = 50 cm) equipped with a LN2-cooled UV-optimized CCD sensor (Princeton Instruments; PyLoN:2KBUV) to acquire UVRR spectra. The "analytical standard" grade anthracene was purchased from Sigma-Aldrich and used without further purification to prepare 100 µM solution in acetonitrile. To minimize the effect of photo-bleaching, the fresh sample was used in each UVRR measurement. The optical power of the tunable UV excitation at the sample was kept constant, and all the UVRR spectra were recorded with integration time of 5 min and five accumulations. For all excitation wavelengths, additional UV Raman spectra of cyclohexane were recorded, and their peak positions were used for calibration of the relative wavenumber axis in the corresponding UVRR spectra of anthracene solution. A spectrally isolated off-resonance Raman (C≡N) peak around 2250 cm^{-1} of the acetonitrile was used as an internal reference for the normalization of the intensity scale of the UVRR spectra.

The UV absorption spectrum of anthracene solution in acetonitrile was measured on a commercial UV–vis photospectrometer (PerkinElmer: Lambda 650) using a fused silica cuvette (Hellma, d = 2 mm).

All calculations were done at the DFT level and its time-dependent extension (TD-DFT) for excited electronic states (the first 20 excited electronic states were considered). Equilibrium geometries were obtained using very tight convergence criteria (maximum forces and displacements were smaller than 5×10^{-6} Hartree/Bohr and 2×10^{-5} Å). Wavenumbers and normal modes in both ground and electronic excited states were computed by analytic force constants, as implemented in Gaussian 16.[42] Solvent effects from acetonitrile were accounted for using the integral equation formalism of the PCM (IEF-PCM[20]). The quality of PCM to represent the solvent effects was checked by comparing the measured and simulated one-photon absorption spectra of anthracene in different solvents (acetonitrile, dichloromethane, and cyclohexane), showing similar features between solvents and a good agreement between theory and experiment (see Figure S1). Most computations employ the B3LYP exchange correlation functional in conjunction with the SNSD[43] basis set, a basis set built upon 6-31G(d,p), with emphasis on the description of spectroscopic observables. The importance of long-range effects was checked against CAM-B3LYP (see Figure S2).

Vibrationally resolved one-photon absorption spectra were computed using the time-dependent formulation as described in Ref.,[44] at $T = 298$ K. The default parameters as implemented in Gaussian 16 were used for the calculation of the autocorrelation function, that is, a total time of 10^{-10} s discretized in 2^{18} points. Having confirmed that the temperature effects had negligible impact on the band shape, the sum-over-states approach was used to generate the stick spectrum and to extract band assignment information, using the class-based prescreening described in Refs.[45–47] A maximum of 20 quanta was considered for each mode in the calculation of the overtones (class 1) and up to 13 for each mode in binary combinations (class 2). The prescreening scheme was used for combinations involving more simultaneously excited modes (up to 7), with a maximum of 10^8 transitions per class. The quality of the prescreening scheme was checked against the total intensity computed by mean of analytic sum rule, and a convergence above 99% was reached (99.99% for FCHT and 100% for FC), which confirms the excellent performance of the prescreening for such a rigid system. For RR, the time-dependent formulation was used to compute the spectrum involving only fundamental final states, and to confirm the quality of the sum-over-state approach, computing the cross-correlation function over 10^{-12} s (same number of point; see Ref.[29] for details). For all RR calculations, the damping constant was fixed at 150 cm^{-1}, based on previous calculations.[29] To compute the RR involving nonfundamental bands in the final state, the more flexible time-independent approach was used, with the same parameters for the prescreening in the intermediate state as in OPA.

For anharmonic calculations, two variants of second-order vibrational perturbation theory (VPT2) were

used.[24] The vibrational normal Raman spectrum was computed with the generalized VPT2 (GVPT2) scheme, which offers a robust treatment of Fermi resonances and the inclusion of Darling–Dennison couplings. However, the final variational step introduces a transformation, so the resulting states can be significantly different from the harmonic ones. This impedes the use of such method to correct the energies of the vibrational states in vibronic calculations, because the underlying model is still the harmonic approximation. For this reason, the hybrid degeneracy-corrected VPT2 (HDCPT2), as described in Ref.,[48] was also employed in the ground state. This model has the advantage of correcting efficiently the problem of Fermi resonances, without the need for empirical thresholds and a variational step to correct the missing contributions from the discarded resonances. Thanks to these features, the anharmonic fundamental energies can be directly associated to their harmonic counterparts and a scaling factor can be computed to correct the harmonic wavenumbers in the final state, following the strategy described in Ref.[49] The anharmonic force constants (third and semidiagonal fourth derivatives of the energy) were generated by numerical differentiations of analytic second derivatives obtained at displaced geometry along the normal coordinates (step of $\delta Q = 0.01 \sqrt{\text{amu} \cdot \text{Å}}$).

ACKNOWLEDGEMENTS

DATA AVAILABILITY STATEMENT
The data that support the findings of this study are available from the corresponding author upon reasonable request.

ORCID
Tim Holtum https://orcid.org/0000-0002-5490-4991
Julien Bloino https://orcid.org/0000-0003-4245-4695
Vikas Kumar https://orcid.org/0000-0002-7335-0824
Vincenzo Barone https://orcid.org/0000-0001-6420-4107
Sebastian Schlücker https://orcid.org/0000-0003-4790-4616

REFERENCES
[1] S. A. Asher, C. R. Johnson, J. Murtaugh, *Rev. Sci. Instrum.* **1983**, *54*, 1657.
[2] S. P. A. Fodor, R. P. Rava, T. R. Hays, T. G. Spiro, *J. Am. Chem. Soc.* **1985**, *107*, 1520.
[3] J. B. Ames, M. Ros, J. Raap, J. Lugtenburg, R. A. Mathies, *Biochemistry* **1992**, *31*, 5328.
[4] S. A. Asher, *Anal. Chem.* **1993**, *65*, 59A.
[5] S. A. Asher, *Anal. Chem.* **1984**, *56*, 720.
[6] C. R. Johnson, M. Ludwig, S. O'Donnell, S. A. Asher, *J. Am. Chem. Soc.* **1984**, *106*, 5008.
[7] K. M. Sanchez, G. Kang, B. Wu, J. E. Kim, *Biophys. J.* **2011**, *100*, 2121.
[8] A. Bröermann, H.-J. Steinhoff, S. Schlücker, *J. Mol. Struct.* **2014**, *1073*, 77.
[9] S. A. Oladepo, K. Xiong, Z. Hong, S. A. Asher, J. Handen, I. K. Lednev, *Chem. Rev.* **2012**, *112*, 2604.
[10] I. López-Peña, B. S. Leigh, D. E. Schlamadinger, J. E. Kim, *Biochemistry* **2015**, *54*, 4770.
[11] L. Chinsky, P. Y. Turpin, *Biopolymers* **1982**, *21*, 277.
[12] S. P. A. Fodor, T. G. Spiro, *J. Am. Chem. Soc.* **1986**, *108*, 3198.
[13] B. Küstner, C. Schmuck, P. Wich, C. Jehn, S. K. Srivastava, S. Schlücker, *Phys. Chem. Chem. Phys.* **2007**, *9*, 4598.
[14] S. Niebling, H. Y. Kuchelmeister, C. Schmuck, S. Schlücker, *Chem. Comm.* **2011**, *47*, 568.
[15] B. Zakeri, S. Niebling, A. G. Martínéz, P. Sokkar, E. Sanchez-Garcia, C. Schmuck, S. Schlücker, *Phys. Chem. Chem. Phys.* **2018**, *20*, 1817.
[16] T. Holtum, V. Kumar, D. Sebena, J. Voskuhl, S. Schlücker, *Beilstein J. Org. Chem.* **2020**, *16*, 2911.
[17] V. Kumar, T. Holtum, J. Voskuhl, M. Giese, T. Schrader, S. Schlücker, *Spectrochim. Acta, Part A* **2021**, *254*, 119622.
[18] C. Li, P. C. Stair, in *11th International Congress on Catalysis - 40th Anniversary*, (Eds: J. W. Hightower, W. Nicholas Delgass, E. Iglesia, A. T. Bell) Vol. 101, Elsevier, Amsterdam (Netherlands) **1996** 881.
[19] S. Jin, Z. Feng, F. Fan, C. Li, *Catal. Lett.* **2015**, *145*, 468.
[20] E. Cances, B. Mennucci, J. Tomasi, *J. Chem. Phys.* **1997**, *107*, 3032.
[21] J. Tomasi, B. Mennucci, R. Cammi, *Chem. Rev.* **2005**, *105*, 2999.
[22] S. Montero, *J. Chem. Phys.* **1982**, *77*, 23.
[23] V. Barone, *J. Chem. Phys.* **2004**, *120*, 3059.
[24] J. Bloino, V. Barone, *J. Phys. Chem.* **2012**, *136*, 124108.
[25] D. A. Long, *The Raman Effect*, Wiley, Chichester (England) **2002**.
[26] L. Jensen, L. L. Zhao, J. Autschbach, G. C. Schatz, *J. Chem. Phys.* **2005**, *123*, 174110.
[27] F. Santoro, C. Cappelli, V. Barone, *J. Chem. Theory Comput.* **2011**, *7*, 1824.
[28] F. Egidi, J. Bloino, C. Cappelli, V. Barone, *J. Chem. Theory Comput.* **2014**, *10*, 346.
[29] A. Baiardi, J. Bloino, V. Barone, *J. Chem. Phys.* **2014**, *141*, 114108.
[30] M. Dierksen, S. Grimme, *J. Chem. Phys.* **2004**, *120*, 3544.
[31] M. Dierksen, S. Grimme, *J. Chem. Phys.* **2005**, *122*, 244101.
[32] T. Sattasathuchana, J. S. Siegel, K. K. Baldridge, *J. Chem. Theory Comput.* **2020**, *16*, 4521.
[33] J. Huh, R. Berger, *Faraday Discuss.* **2011**, *150*, 363.

[34] J. Bloino, *J. Phys. Chem. A* **2015**, *119*, 5269.

[35] J. Bloino, M. Biczysko. in *Reference Module in Chemistry, Molecular Sciences and Chemical Engineering*, Elsevier, Amsterdam (Netherlands) **2015**.

[36] B. A. McGuire, R. A. Loomis, A. M. Burkhardt, K. L. K. Lee, C. N. Shingledecker, S. B. Charnley, I. R. Cooke, M. A. Cordiner, E. Herbst, S. Kalenskii, M. A. Siebert, E. R. Willis, C. Xue, A. J. Remijan, M. C. McCarthy, *Science* **2021**, *371*, 1265.

[37] A. G. G. M. Tielens, *Annu. Rev. Astron. Astrophys.* **2008**, *46*, 289.

[38] A. C. Albrecht, *J. Chem. Phys.* **1961**, *34*, 1476.

[39] P. F. Loos, A. Scemama, D. Jacquemin, *J. Phys. Chem. Lett.* **2020**, *11*, 2374.

[40] C. Puzzarini, J. Bloino, N. Tasinato, V. Barone, *Chem. Rev.* **2019**, *119*, 8131.

[41] V. Kumar, T. Holtum, D. Sebena, M. Giese, J. Voskuhl, S. Schlücker, *Spectrochim. Acta, Part A* **2021**, *250*, 119359.

[42] M. J. Frisch, G. W. Trucks, H. B. Schlegel, G. E. Scuseria, M. A. Robb, J. R. Cheeseman, G. Scalmani, V. Barone, G. A. Petersson, H. Nakatsuji, X. Li, M. Caricato, A. V. Marenich, J. Bloino, B. G. Janesko, R. Gomperts, B. Mennucci, H. P. Hratchian, J. V. Ortiz, A. F. Izmaylov, J. L. Sonnenberg, D. Williams-Young, F. Ding, F. Lipparini, F. Egidi, J. Goings, B. Peng, A. Petrone, T. Henderson, D. Ranasinghe, V. G. Zakrzewski, J. Gao, N. Rega, G. Zheng, W. Liang, M. Hada, M. Ehara, K. Toyota, R. Fukuda, J. Hasegawa, M. Ishida, T. Nakajima, Y. Honda, O. Kitao, H. Nakai, T. Vreven, K. Throssell, J. A. Montgomery Jr., J. E. Peralta, F. Ogliaro, M. J. Bearpark, J. J. Heyd, E. N. Brothers, K. N. Kudin, V. N. Staroverov, T. A. Keith, R. Kobayashi, J. Normand, K. Raghavachari, A. P. Rendell, J. C. Burant, S. S. Iyengar, J. Tomasi, M. Cossi, J. M. Millam, M. Klene, C. Adamo, R. Cammi, J. W. Ochterski, R. L. Martin, K. Morokuma, O. Farkas, J. B. Foresman, D. J. Fox, *Gaussian 16 Revision A.03*, Gaussian Inc., Wallingford (CT) **2016**.

[43] Double and triple-ζ basis sets of SNS family. Available at: https://smart.sns.it/?pag=download

[44] A. Baiardi, J. Bloino, V. Barone, *J. Chem. Theory Comput.* **2013**, *9*, 4097.

[45] F. Santoro, R. Improta, A. Lami, J. Bloino, V. Barone, *J. Chem. Phys.* **2007**, *126*, 084509.

[46] F. Santoro, A. Lami, R. Improta, J. Bloino, V. Barone, *J. Chem. Phys.* **2008**, *128*, 224311.

[47] J. Bloino, M. Biczysko, F. Santoro, V. Barone, *J. Chem. Theory Comput.* **2010**, *6*, 1256.

[48] J. Bloino, M. Biczysko, V. Barone, *J. Chem. Theory Comput.* **2012**, *8*, 1015.

[49] J. Bloino, M. Biczysko, O. Crescenzi, V. Barone, *J. Phys. Chem.* **2008**, *128*, 244105.

SUPPORTING INFORMATION

Additional supporting information may be found in the online version of the article at the publisher's website.